



**HAL**  
open science

# Tetrahedral Complexity in Amorphous Networks: A Possible Clue for the Unique Properties of Phase-Change Materials

Matthieu Micoulaut, Hugo Flores-Ruiz, Annie Pradel, Andrea Piarristeguy

► **To cite this version:**

Matthieu Micoulaut, Hugo Flores-Ruiz, Annie Pradel, Andrea Piarristeguy. Tetrahedral Complexity in Amorphous Networks: A Possible Clue for the Unique Properties of Phase-Change Materials. *physica status solidi (RRL) - Rapid Research Letters*, 2021, Phase-Change and Ovonic Materials, 15 (3), pp.2000490. 10.1002/pssr.202000490 . hal-03043696

**HAL Id: hal-03043696**

**<https://hal.science/hal-03043696>**

Submitted on 9 Aug 2021

**HAL** is a multi-disciplinary open access archive for the deposit and dissemination of scientific research documents, whether they are published or not. The documents may come from teaching and research institutions in France or abroad, or from public or private research centers.

L'archive ouverte pluridisciplinaire **HAL**, est destinée au dépôt et à la diffusion de documents scientifiques de niveau recherche, publiés ou non, émanant des établissements d'enseignement et de recherche français ou étrangers, des laboratoires publics ou privés.

# Tetrahedral Complexity in Amorphous Networks: A Possible Clue for the Unique Properties of Phase-Change Materials

Matthieu Micoulaut,\* Hugo Flores-Ruiz, Annie Pradel, and Andrea Piarristeguy

A typical binary amorphous telluride  $\text{GeTe}_2$  is investigated from the first principles molecular dynamics simulations. After a comparison with chemical analogs from neutron or X-ray diffraction experiments, such as  $\text{GeO}_2$  or  $\text{GeSe}_2$ , the structure of this material is focused by examining real and reciprocal space properties. It is found that the base geometrical motifs of the germanium atom can be either in tetrahedral or in defected coordinations involving pyramidal units. A review of previous results for other compositions reveals that such binary Ge tellurides contain soft tetrahedra, at variance with lighter chalcogenides, such as Ge–S and Ge–Se, and are characterized by an increased angular bending motion (typically  $20^\circ$ ) as compared with, e.g., Ge–S ( $5^\circ$ ). In addition, for amorphous Ge-rich materials,  $\text{GeTe}_2$  and  $\text{GeTe}$ , a secondary tetrahedral geometry appears, related to the presence of Ge–Ge bonds, having a larger mean angle of about  $125^\circ$ . These typical features not only relate to characteristics observed from scattering experiments but may also be a crucial feature for the understanding of the phase-change phenomena.

or optical contrast between a crystalline and an amorphous phase, as well as the fast recrystallization of the amorphous phase. On PC properties and recording, special emphasis is made on short crystallization times, on the optical or electrical contrast between the amorphous and the crystalline phase,<sup>[2]</sup> on the reversibility between both phases upon a large number of phase-change cycles, and on the high thermal stability. Over the years, extensive investigations as a function of composition or alloying elements have led to the recognition that such important properties and performances are being optimized along the  $\text{GeTe} - \text{Sb}_2\text{Te}_3$  join in the ternary Ge–Sb–Te system (GST). In this search for optimal performances, the key material has turned to be  $\text{GeTe}$  or  $\text{Ge}_2\text{Sb}_2\text{Te}_5$ , one of the very first PCM used for enhanced storage capacities<sup>[2]</sup> close to the  $100\text{GB}/\text{cm}^2$  domain.

Over the past two decades, phase-change materials (PCM) have received a huge attention with various technological applications ranging from optical discs, such as DVD-RW or blue-ray discs, to phase-change memory (PC-RAM), including more recent opportunities as all-photonic memories and flexible displays with nanopixel resolution.<sup>[1]</sup> These applications build mainly on unique properties of the PCM that use the important electrical

Of special interest is the nature of the Ge geometry as it has been suggested that the PC mechanism is driven by switching between an octahedral (O) site in the crystalline state to a fourfold tetrahedral (T) site in the amorphous one,<sup>[3]</sup> as it is known that external conditions (light, current, and pressure) lead to an increase in the atomic bond lengths,<sup>[4,5]</sup> which appears to be one of the very obvious mechanisms able to accommodate the electronic repulsion induced by a reduction of the bond angle from  $109^\circ$  to about  $90^\circ$ . While such a simple picture might not be fully valid, a certain number of comments should be made. First, one neglects the possibility to have homopolar Ge–Ge bonds, but these are obviously present in PCM having the appropriate compositions<sup>[6]</sup> and also might drive the tendency to form T–Ge. While a certain number of contributions using density functional theory (DFT)-based simulations have found that the population of such (T) motifs represents minority sites,<sup>[7–9]</sup> it should be emphasized that the theoretical conclusions were based on electronic schemes that led to a spurious overestimation of the Ge–Te bond length, typical of octahedral geometries. In addition, the methods of estimation of the tetrahedral population  $\eta$  were in part inaccurate, and recently, a rigorous approach has been introduced to estimate  $\eta$ .<sup>[10]</sup> In parallel, improved DFT schemes (i.e., DFT-D2) using the inclusion of empirical dispersion forces have been used,<sup>[11]</sup> and these have been found to substantially improve the structural description and to reduce the Ge–Te bond length; this statement is valid for a variety of

Dr. M. Micoulaut  
Physique Théorique de la Matière Condensée  
Sorbonne Université  
CNRS UMR  
7600, Boite 121, 4 place Jussieu, 75252 Paris, Cedex 05, France  
E-mail: mmi@lptl.jussieu.fr

Dr. H. Flores-Ruiz  
Departamento de Ciencias Naturales y Exactas, CUValles  
Universidad de Guadalajara  
Carr. Guadalajara-Ameca km 45.5, Ameca, Jalisco 46600, México

Dr. A. Pradel, Dr. A. Piarristeguy  
ENSCM  
ICGM  
Univ Montpellier  
CNRS  
Montpellier, France

The ORCID identification number(s) for the author(s) of this article can be found under <https://doi.org/10.1002/pssr.202000490>.

DOI: 10.1002/pssr.202000490

1 PCM in the liquid and amorphous phase.<sup>[12–15]</sup> The main  
2 outcome from these recent studies is that the structure of PC  
3 tellurides is dominated by T–Ge, a conclusion already made  
4 on different Ge–Te glasses from the simple inspection of the  
5 experimental pair correlation function, which displays similar-  
6 ties with one of the tetrahedral chalcogenides and a global mini-  
7 mum defining well-separated shells of neighbors.<sup>[16]</sup> Mössbauer  
8 spectroscopy of <sup>119</sup>Sn substituted tellurides, which probe the  
9 local geometry in amorphous tellurides, tetrahedral versus octa-  
10 hedral, also provides evidence that the population of T–Ge is  
11 much larger than believed from DFT-based simulations.<sup>[10,17]</sup>  
12 Can this structural picture be reconciled with the fact that  
13 only a limited degree of sp<sup>3</sup> hybridization must be present to  
14 enable resonance p-electron for phase switching? This question  
15 continues to be of great interest, both from the fundamental  
16 viewpoint and the applied one.

17 In the present contribution, we continue to explore this issue  
18 by examining the structural properties of a certain composition  
19 in the Ge–Te binary system, that is, GeTe<sub>2</sub>. Our motivation is  
20 driven by the fact that this material is a chemical analog of  
21 germania or lighter chalcogenides (e.g., GeSe<sub>2</sub>), which not only  
22 easily form bulk glasses but also display a fully tetrahedral  
23 network. **Figure 1** highlights the effect of Group-VI substitution  
24 on the structural properties of GeX<sub>2</sub> glasses (X = O, S, Se, Te) by  
25 representing the experimental total structure factor *S(k)* accessed

from neutron diffraction (ND) or X-ray diffraction (XRD), 1  
together with results from simulations. The examination of 2  
the substitution of Group-VI atoms permits one to track what 3  
aspects of structural order at short and intermediate ranges 4  
are impacted as one moves from the tetrahedral GeO<sub>2</sub> to the 5  
GeTe<sub>2</sub> made of probable mixed atomic geometries. To access 6  
to such information for the present telluride, we perform density 7  
functional-based simulations to extract relevant information and 8  
compare results with other compositions in the Ge–Te binary to 9  
finally establish the tetrahedral fraction  $\eta$  with Ge content. 10  
Results also indicate that compositions used for phase-change 11  
applications (i.e., GeTe) display tetrahedral geometries with 12  
minority populations having an angle larger than 109°, and these 13  
involve a homopolar Ge–Ge bond. 14

To assess our conclusions, we have generated a certain num- 15  
ber of different structural models of amorphous GeTe<sub>2</sub>, and 16  
these were obtained by quenching (10 K ps<sup>−1</sup>) three independent 17  
configurations of equilibrated liquids obtained at 820 K, and 18  
accumulating trajectories over 30 ps each. Such liquids are super- 19  
cooled given that the liquidus temperature  $T_L > 820$  K and can 20  
also be considered as equilibrated from the viewpoint of simu- 21  
lations, because the total energy of the system is merely constant 22  
and displays diffusive regime at large time. Note that a 920 K 23  
liquid has also been obtained and is used in the following 24  
discussion. Molecular dynamics (MD) simulations of Car- 25  
Parrinello type were performed on 200-atom systems in a cubic 26  
box with periodic boundary conditions and a density equal to 27  
experimental ones.<sup>[16]</sup> The methodology of the simulations has 28  
been given elsewhere for other compositions in the Ge–Te 29  
binary, and we refer the readers to the relevant reference for 30  
details.<sup>[10]</sup> In short, the electronic structure has been described 31  
within DFT-D2 and evolved self-consistently during the motion 32  
(time step  $\Delta t = 0.12$  fs) using a generalized gradient approxima- 33  
tion. Valence electrons were treated explicitly, in conjunction 34  
with Troullier–Martins norm-conserving pseudopotentials 35  
using a plane-wave basis set with an energy cutoff of 20 Ry. 36  
The exchange–correlation functional was taken from Perdew, 37  
Burke, and Ernzerhof (PBEsol)<sup>[18]</sup> together with the inclusion of 38  
dispersion forces<sup>[19]</sup> to improve the local structure (bond length) 39  
with respect to experimental findings. 40

We first represent in Figure 1 the structure factor *S(k)* of the 41  
simulated GeTe<sub>2</sub> using 42

$$S_{ij}(k) = \left\langle \sum_{n=1}^{N_i} \sum_{m=1}^{N_j} e^{-ik(r_n - r_m)} \right\rangle \quad (1) \quad \text{Q4}$$

and 43

$$S(k) = \frac{\sum_{ij} x_i x_j \alpha_i \alpha_j S_{ij}(k)}{\sum_{ij} x_i x_j \alpha_i \alpha_j} \quad (2)$$

where  $x_i$  represents the atomic fraction of atom *i*, and  $\alpha_i$  44  
either the atomic form factor in an XRD experiment or the 45  
neutron coherence length in a neutron diffusion experiment. 46  
Equation (2) is then compared with scattering results<sup>[16]</sup> and with 47  
the results from chemical analogs of the form GeX<sub>2</sub> obtained 48  
either experimentally (X = O, S, Se<sup>[20–22]</sup>) or theoretically.<sup>[4,23,24]</sup> 49

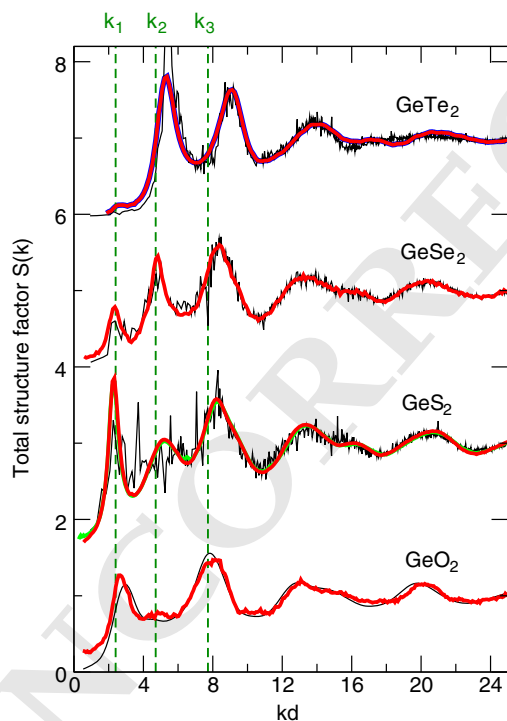


**Figure 1.** Total structure factor *S(k)* for different amorphous chalcogenides rescaled as a function of *kd*, where *d* is the nearest-neighbor distance. Colored curves represent experimental data from XRD or ND, whereas thin black curves are simulation results: GeO<sub>2</sub><sup>[4]</sup> (*d* = 1.73Å, expt.<sup>[20]</sup>), GeS<sub>2</sub><sup>[23]</sup> (*d* = 2.22Å, expt.<sup>[21,51]</sup>), GeSe<sub>2</sub><sup>[24]</sup> (*d* = 2.36Å, expt.<sup>[22]</sup>), and GeTe<sub>2</sub> (*d* = 2.68Å, expt.<sup>[16]</sup>). The blue curve of GeTe<sub>2</sub> is a result from RMC simulations.<sup>[25]</sup> The broken vertical green lines represent typical positions for the first three peaks in network-forming glasses:<sup>[26]</sup> *k*<sub>1</sub>, *k*<sub>2</sub>, and *k*<sub>3</sub>.

1 The represented materials display rather different structures as  
2 GeO<sub>2</sub> is entirely based on corner-sharing (CS) tetrahedra,  
3 whereas both GeS<sub>2</sub> and GeSe<sub>2</sub> have a mixed topology made of  
4 both CS and edge-sharing (ES) tetrahedral.<sup>[24]</sup> The structure  
5 of GeTe<sub>2</sub>, albeit investigated from XRD,<sup>[16]</sup> appears to be  
6 still not fully elucidated, although reverse Monte Carlo (RMC)  
7 methods<sup>[16,25]</sup> have characterized the structure in more detail.  
8 The characterization of the local structure and environment  
9 including the degree of tetrahedral character will be discussed  
10 throughout this contribution.

11 There has been a recent attempt to establish ordering on typi-  
12 cal length scales from scattering functions in tetrahedral materi-  
13 als,<sup>[26]</sup> and these can be summarized in a single plot (Figure 1)  
14 once the  $x$ -axis has been rescaled using the first nearest neighbor  
15 distance  $d = r_{\text{Ge-X}}$  that can be determined either from the full set  
16 of calculated partial pair distribution functions  $g_{ij}(r)$  or from the  
17 resolution of experimental partials using either isotopic substi-  
18 tuted ND<sup>[20,22]</sup> or anomalous X-ray scattering (AXS<sup>[27]</sup>). Once  
19 represented as a function of  $kd$ , the structure factor features three  
20 typical peaks with positions  $k_i d$  that scale as  $k_1 d = 2.3$ ,  
21  $k_2 d = 4.6 - 4.9$ , and  $k_3 d = 5\pi/2 \approx 7.7 - 8.9$  where the first  
22 one is referred to the first sharp diffraction peak (FSDP) found  
23 in a variety of glasses, and the peaks at  $i = 2, 3$  are usually termed  
24 the principal peaks.

25 An inspection of the substitution of the progressive heavier  
26 Group-VI atoms indicates that the peak at  $k_1 d$  (i.e., the FSDP)  
27 tends to vanish when moving from GeO<sub>2</sub> to GeTe<sub>2</sub>, whereas  
28 the opposite trend is acknowledged for the peak at  $k_2 d$ . The peak  
29 at  $k_3 d$  appears to be more or less preserved under chemical  
30 substitution, except a shift to higher  $kd$  for heavier Group-VI  
31 elements. The observed variability underscores obvious changes  
32 in the ordering of length scales.

33 A decomposition into partials for amorphous GeTe<sub>2</sub> (Figure 2)  
34 shows that the first principal peak observed at  $kd \approx 5$  (i.e.,  
35  $k = 2.1 \text{ \AA}^{-1}$ ) arises essentially from all partials but with a larger  
36 contribution arising from Te–Te correlations, and the secondary  
37 principal peak having an approximate contribution of 1:2:1  
38 from Ge–Ge, Te–Te, and Ge–Te, respectively. Note that some  
39 differences emerge from structure models obtained from RMC  
40 fits (blue curves), especially for the Ge–Ge partial, and the other  
41 two DFT calculated functions  $S_{\text{TeTe}}(k)$  and  $S_{\text{GeTe}}(k)$  are globally  
42 compatible with the RMC.<sup>[25]</sup>

43 These features rather compare well with experimental deter-  
44 minations from AXS for a close composition (GeTe<sup>[27]</sup>), and the  
45 determination of relevant partials indicates, indeed, that the prin-  
46 cipal peak at  $\approx 2 \text{ \AA}^{-1}$  is dominated by Te-based correlations,  
47 whereas the one at  $3.5 \text{ \AA}^{-1}$  arises from a more equilibrated  
48 contribution from both Ge and Te.

49 While the peak at  $k_3$  is found for all materials and associated  
50 with nearest-neighbor contacts that correspond to the very first  
51 shell of neighbors,<sup>[28]</sup> the second peak at  $k_2$  is supposed to be  
52 indicative of a bonding scheme assuming directional character  
53 that leads to the formation of tetrahedral motifs.<sup>[26]</sup> This suggests  
54 that the present GeTe<sub>2</sub> is partially tetrahedral but with a Ge  
55 subnetwork that has no long-range correlation given the absence  
56 of the FSDP.

57 It is also instructive to inquire real-space properties, and  
58 Figure 3a shows the computed pair correlation functions of

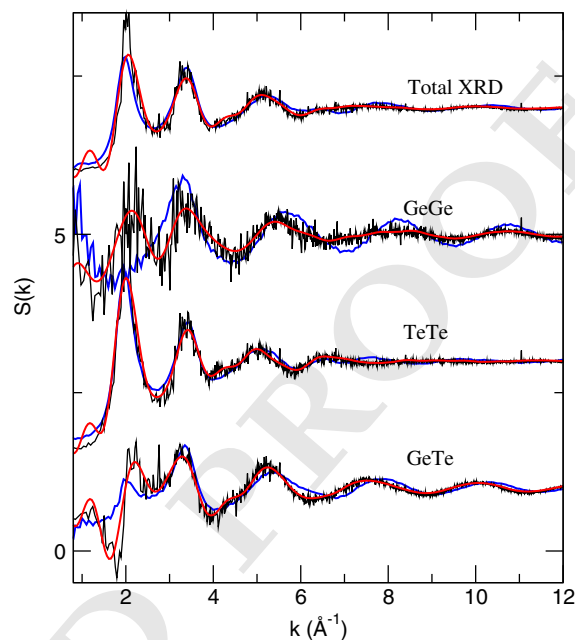
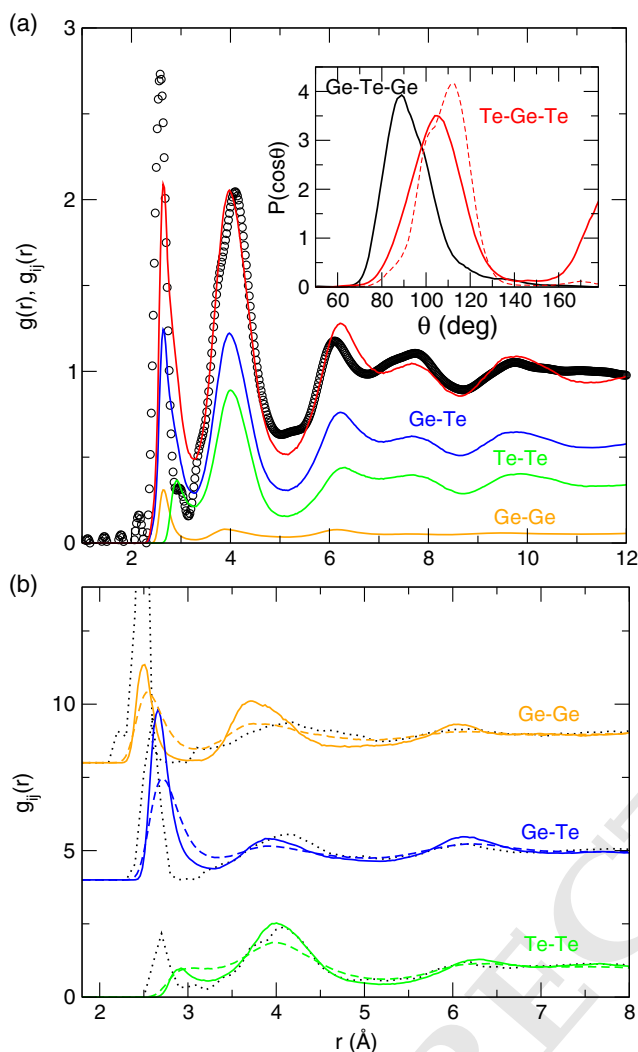


Figure 2. Calculated total structure factor  $S(k)$  and Faber–Ziman-related partials  $S_{ij}(k)$  of amorphous GeTe<sub>2</sub>. Black curves: direct calculation from the trajectories using Equation (1). Red curves: Fourier transform of  $g(r)$  and  $g_{ij}(r)$ . The blue curves correspond to an RMC model of GeTe<sub>2</sub>.<sup>[25]</sup>

GeTe<sub>2</sub>, compared with available XRD measurements from the literature.<sup>[16]</sup>

It appears that the agreement is rather very good at short distances as the main features of the pair distribution function; the main peak at  $2.65 \text{ \AA}$  dominated by Ge–Te correlations (experimentally  $2.61 \text{ \AA}$ <sup>[25]</sup>) is correctly reproduced, as well as the second principal peak arising from the second neighbor shell at  $\approx 4.10 \text{ \AA}$ . This secondary peak actually results from different contributions (Ge–Te and Te–Te) and has been previously found to depend on the Ge content,<sup>[10,25]</sup> but in the present material, the Te–Te correlations essentially arise from vertices of the Ge polyhedra, and the first peak at  $\approx 2.67 \text{ \AA}$  is associated with the remaining Te–Te homopolar bonds. Here, the structure remains, indeed, dominated by such Te–Te and Ge–Te correlations, and the possibility of having Ge–Ge atoms is still small, albeit a typical prepeak featuring the Ge–Ge homopolar bonds is found at  $\approx 2.69 \text{ \AA}$ , i.e., somewhat larger than the corresponding distance found in GeSe<sub>2</sub> ( $2.44 \text{ \AA}$ <sup>[22]</sup>). The Ge–Te distance is found to increase with temperature (from  $2.65$  to  $2.69 \text{ \AA}$  at  $820 \text{ K}$ ), which is compatible with experimental studies in the liquid state,<sup>[29]</sup> albeit the bond distance is slightly underestimated with respect to experimental data ( $2.81 \text{ \AA}$  at  $1023 \text{ K}$ <sup>[30]</sup>). It should also be remarked that some differences with the RMC models<sup>[25]</sup> of amorphous GeTe<sub>2</sub> do appear (Figure 3b), especially for Ge–Ge and Te–Te correlations, and the amplitude of the main peak of the former is much larger than the present calculated one from DFT, which signals an increased Ge–Ge structuration for RMC structures. Similarly, the homopolar Te–Te and the Ge–Te bonds are found to be slightly smaller in RMC models. The combination of both sets of partials leads to a similar total pair



**Figure 3.** a) Calculated total pair correlation function  $g(r)$  (red) together with corresponding weighted partials in amorphous  $\text{GeTe}_2$ . Experimental data from XRD are represented by circles.<sup>[25]</sup> The inset shows the calculated BADs  $P(\cos\theta)$  Ge–Te–Ge (black) and Te–Ge–Te (red) together with a corresponding distribution Se–Ge–Se for  $\text{GeSe}_2$  (broken red line<sup>[24]</sup>). b) Comparison of the calculated functions  $g_{ij}(r)$  (solid lines), the same as panel (a) with corresponding partials obtained in the liquid state (broken colored curves, 920 K) and from RMC (dotted lines<sup>[25]</sup>).

octahedral geometry for Te.<sup>[31]</sup> Conversely, the Ge-centered 1  
bond angle turns out to display a main distribution at 105° 2  
and a tail at 180°, which is the signature of the presence of defect 3  
octahedral geometries. Note that here, we have represented 4  
 $P(\cos\theta) = P(\theta)/\sin\theta$  rather than  $P(\theta)$ , which permits to blow 5  
up the angles found at 180°. In fact, as the infinitesimal area 6  
element during angle calculations in spherical coordinates is 7  
 $\sin\theta d\Phi d\theta$ , as one approaches  $\theta \rightarrow 180^\circ$ , the area goes to zero, 8  
and therefore,  $P(180^\circ) \rightarrow 0$ . We also recall that the inclusion 9  
of dispersion forces tends to shift the Te–Ge–Te BAD to larger 10  
angles and to an increased tetrahedral character.<sup>[14]</sup> 11

To investigate the angular motion around the Ge atom, we 12  
use algorithms, which convert the bond-bending motion into a 13  
topological constraint.<sup>[32,33]</sup> Such a counting is based on partial 14  
bond angle distributions (PBADs)  $P(\theta_{ij})$  that is defined from a set 15  
of neighbors. From a given trajectory, we first select  $N$  first neighbors, 16  
which lead to  $N(N-1)/2$  possible angles labeled as  $i0j$  17  
with  $(i,j) = \{1..N\}$  and 0 the central Ge atom; i.e., one has 18  
102, 103, etc. From such PBADs, a corresponding first moment 19  
 $\bar{\theta}$  and second moment (standard deviation)  $\sigma_{\theta_{ij}}$  can be calculated 20  
for each distribution, and this provides a measure of average angle 21  
and its excursion, which is related to the bond-bending 22  
interaction strength.<sup>[34]</sup> Such methods have permitted to estimate 23  
network rigidity in glasses and other complex materials as a function 24  
of thermodynamic conditions.<sup>[35,36]</sup> In the forthcoming, we 25  
have set  $N = 6$ , and this leads to 15 possible PBADs out of which 26  
different  $\bar{\theta}$  and  $\sigma_{\theta_{ij}}$  ( $\sigma_\theta$  in the forthcoming) have been calculated. 27

To check for the degree of rigidity of the geometrical unit, one 28  
represents  $\sigma_\theta(\bar{\theta})$  for different systems. In silica where the  $\text{SiO}_{4/2}$  29  
tetrahedra are known to act as a rigid unit mode<sup>[37]</sup> and where the 30  
disordered structure of the network is achieved from a variety 31  
of angles for the bridging oxygen, such a representation leads 32  
to data found at  $\bar{\theta} = 109^\circ$  only for angles  $i0j$  with  $i,j \leq 4$  that 33  
is also acknowledged in corresponding silicates of the form 34  
 $\text{Na}_2\text{O} - \text{SiO}_2$  (SN; **Figure 4**), and such angles, furthermore, display 35  
an equivalent and low value for the corresponding standard 36  
deviation  $\sigma_\theta$  (5°). The same behavior holds for germania 37  
( $\text{GeO}_2$ )<sup>[34]</sup> or for window glass<sup>[38]</sup> (SCN; **Figure 4**). 38

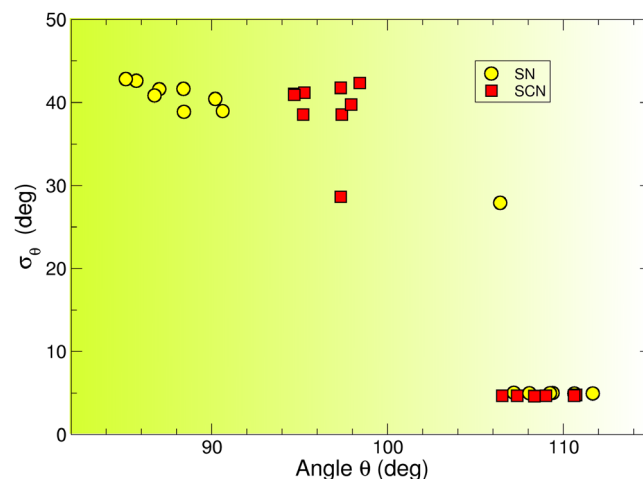


**Figure 4.** Plot of  $\sigma_\theta(\bar{\theta})$  for the silicon atom calculated for a sodium silicate (SN<sup>[32]</sup>) and in window glass  $\text{CaO} - \text{Na}_2\text{O} - \text{SiO}_2$  (SCN<sup>[38]</sup>).

1 correlation function. The coordination numbers obtained at the 2  
minimum of the pair correlation function ( $r_m = 3.27\text{\AA}$ ) are equal 3  
to  $n_{\text{Ge}} = 4.3$  and  $n_{\text{Te}} = 2.7$ ; i.e., typical numbers found at other 4  
compositions in these Ge–Te mixtures<sup>[10,14]</sup> that underscore 5  
1) the increased Te coordination number with respect to the octet 6  
(8-N) rule encountered in the other  $\text{GeX}_2$  materials and 2) the 7  
increased Ge coordination number with respect to its expected 8  
value of 4 and results from a mixed population of tetrahedra 9  
and higher coordinated  $n_{\text{Ge}} > 4$  defect octahedral geometries. 10  
We now concentrate on angles. The bond angle distributions 11  
(BADs) Ge–Te–Ge and Te–Ge–Te are represented in the inset 12  
of Figure 3a and show that the Te-centered angles involve an 13  
angle of about 90°, consistently with the reported defect

1 In contrast, angles involving atoms beyond the first shell of  
2 neighbors lead to larger bond-bending motions due to the  
3 increased distances between the central atom at the chosen  
4  $(i, j)$  with  $4 \leq i, j \leq N$ . This leads to a broad distribution for  
5 the corresponding average angle  $\bar{\theta}$ , which is found in the  
6 range between  $90^\circ \leq \bar{\theta} \leq 105^\circ$ . Such angles are, furthermore,  
7 characterized by a large angular standard deviation ( $\sigma_\theta \simeq 40^\circ$ )  
8 and are not considered here, given that they do not contribute  
9 to the characterization of the short-range order.

10 **Figure 5** now represents the same quantity for binary germa-  
11 nium chalcogenides Ge-X with changing composition ( $X = S, Se,$   
12  $Te$ ). Noticeable features can be detected in the region of interest  
13 ( $\bar{\theta} \simeq 109^\circ, \sigma_\theta \simeq 8 - 20^\circ$ ). Germanium sulfides<sup>[23]</sup> exhibit a simi-  
14 lar trend to the one determined for the oxides; i.e., whatever the  
15 considered composition smaller than the stoichiometric  $GeS_2$   
16 ( $Ge_xS_{100-x}, x \leq 1/3$ ), the  $GeS_{4/2}$  tetrahedra appear to be well  
17 defined and rigid because of a low value for the angular excursion  
18 ( $\sigma_\theta \simeq 8^\circ$ ) that is sharply centered around  $\bar{\theta} \simeq 109^\circ$ . An almost  
19 similar situation is encountered in  $Ge_xSe_{100-x}$  selenides, and  
20 here also,  $\sigma_\theta$  appears to be low for the angles defining the Ge  
21 tetrahedron, except for compositions satisfying  $x \geq 33.3\%$   
22 (not shown here). Here, it was found that the part of the increas-  
23 ing stress imposed by Ge additional cross-links can be released

by softening of the angular constraints, which manifests by an  
increased bending motion inside the tetrahedra<sup>[24]</sup> as also  
detected in the liquid phase when thermal activation softens  
bending interactions.<sup>[23]</sup>

The situation is dramatically changed in Ge-Te binary alloys.  
A representation for various compounds recently investi-  
gated<sup>[10,14]</sup> including the present  $GeTe_2$  indicates that angles  
around the Ge atoms experience wider angular motions, and this  
increases  $\sigma_\theta$  to about  $15 - 20^\circ$  indicative of soft geometrical unit  
at variance with the rigid unit mode encountered in silicas.<sup>[37]</sup>

A representation of different PCM previously investigated<sup>[39]</sup>  
can be plotted to provide some perspective (**Figure 6**). It is seen  
that PCM (e.g.,  $Ge_1Sb_2Te_4$  [GST124]) are characterized by large  
angular excursions ( $10^\circ - 25^\circ$ ) and angles that are somewhat  
smaller than the tetrahedral value but are larger than the typical  
value of pyramidal geometries ( $98^\circ$ ) typical of Group-V elements,  
such as  $As_2Se_3$ . For the tellurides, it is, furthermore, seen that as  
averages are performed over the whole system, angles  $\bar{\theta}$  (i.e., first  
moments of the PBADS) involving the first four neighbors of the  
Ge atom span between the two limiting values of  $98^\circ$  and  $109^\circ$ .

Using such angular constraints, a recent method permits to  
rigorously extract the fraction of Ge tetrahedra.<sup>[10]</sup> The detection  
and quantification of tetrahedral germanium can be made from  
the previously introduced method but instead of ensemble  
averaging to obtain, e.g., Figure 5, one performs a selection of  
individual Ge atoms with a rule based on angular standard devi-  
ations. This has the advantage to focus on angular excursions  
only, rather than working directly on angles, which span over  
a restricted domain. Angles are followed individually during  
the simulation from the  $N(N-1)/2$  possible triplets  $i-Ge-j$   
defined by a set  $(i, j)$  of  $N$  first neighbors. If the calculated number  
of low standard deviations around such atoms is six, a tetrahe-  
dron is identified, because this geometry is defined by six rigid

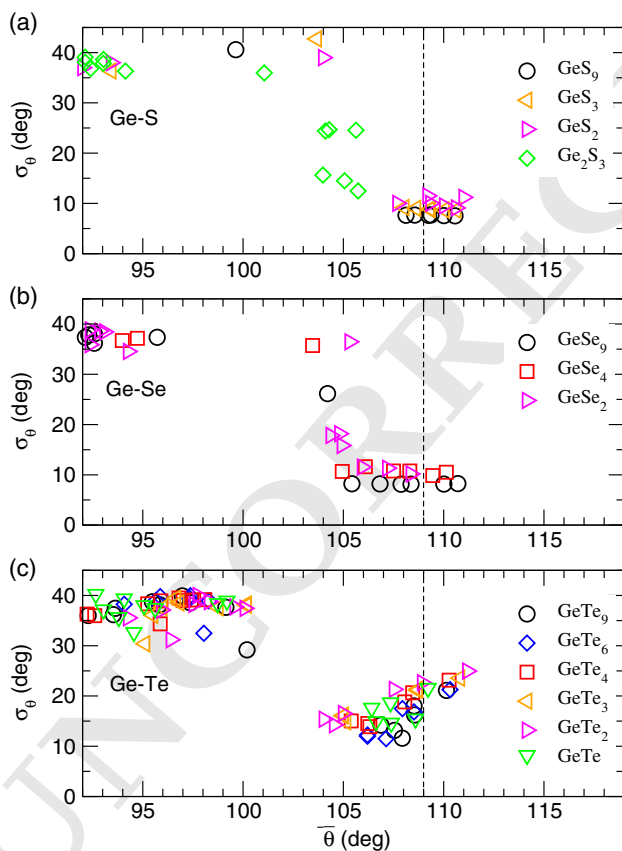


**Figure 5.** Measure of the Ge angular excursion  $\sigma_\theta(\bar{\theta})$  in binary Ge-X chalcogenides. a)  $X=S$  from simulations published in the previous study.<sup>[23]</sup> b)  $X=Se$  from the previous study<sup>[24]</sup> and c)  $X=Te$  from the previous studies<sup>[10,14]</sup> and the present work. The broken vertical line represents the value of the tetrahedral angle.

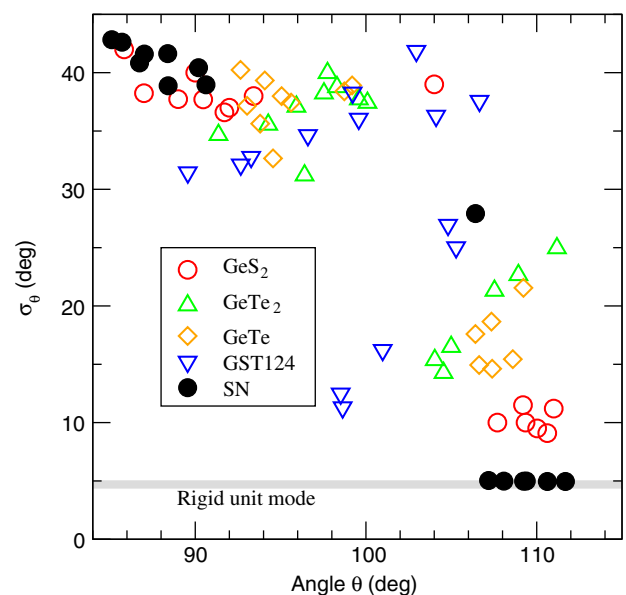


**Figure 6.** Comparison of the Ge angular excursion  $\sigma_\theta(\theta)$  in different phase-change alloys, compared with reference materials (SN, the same as in Figure 4).

1 angles that give rise to corresponding low standard deviations  
2 with associated angles that are all close to  $109^\circ$ .

3 Averages over the entire system for such identified Ge atoms  
4 then lead to a BAD that has the property of having six rigid angles  
5 and centered around  $109^\circ$  (black curve, Figure 7).

6 This distribution for  $\text{GeTe}_2$  is centered at an angle that is  
7 exactly equal to the tetrahedral angle as already acknowledged  
8 for  $\text{GeTe}$ .<sup>[14]</sup> Interestingly, the (T) distribution exhibits a tail at  
9 large  $\theta$  that is not obtained in the corresponding selenide  
10 glass,<sup>[24]</sup> and it signals that tetrahedral Ge atoms display two  
11 distinct populations in this  $\text{GeTe}_2$  material as the six constrained  
12 angles can also experience angular excursions that are larger than  
13 the average  $109^\circ$ , i.e., in the domain between  $120^\circ \leq \theta \leq 160^\circ$ .

14 The residual distribution (nT) has the following properties  
15 (red curve, Figure 7). It is centered at  $\bar{\theta} \approx 98^\circ$ , i.e., typical of a  
16 pyramid with a triangular basis having the Te—Te bonds as  
17 edges, and a Ge at the remaining vertex, similar to the pyramidal  
18 geometry found in  $\text{As}_2\text{Se}_3$  for which three rigid angles are  
19 obtained.<sup>[33]</sup> In the present  $\text{GeTe}_2$ , similar findings are obtained,  
20 and the (nT) is, indeed, also characterized by three rigid angles  
21 with  $\sigma_{\theta ij} \approx 15^\circ$ . Note that possible additional longer bonds do  
22 exist, but these do not constrain the geometry as they involve  
23  $\sigma_{\theta ij} \approx 30^\circ - 40^\circ$ .

24 Finally, the fraction  $\eta$  of tetrahedral Ge can be calculated from  
25 the number of atoms fulfilling six standard deviations with a  
26 low value, and for the present  $\text{GeTe}_2$ , we find  $\eta = 55.0 \pm 1.0$   
27 in amorphous phase. This value is similar to numbers previously  
28 found at close compositions ( $\text{GeTe}_4$ ,  $\eta = 54.6\%$ <sup>[10]</sup>).

29 The results obtained for  $\text{GeTe}_2$  are now put in perspective with  
30 previous ones obtained for other compositions in this Ge—Te  
31 binary.

32 **Figure 8** represents the obtained evolution of the tetrahedral  
33 population in  $\text{Ge}_x\text{Te}_{100-x}$  as a function of Ge content  $x$ . It shows  
34 that chalcogen-rich and Ge-rich materials contain a large amount  
35 of tetrahedral Ge, of about 60–65%. At large Ge content, the  
36 enhancement of the (T) population is known to be driven by  
37 the presence of homopolar bonds, which lead to energetically  
38 more favorable structures in (T) geometry,<sup>[6]</sup> whereas the  
39 increased presence of such motifs at low  $x$  seems compatible

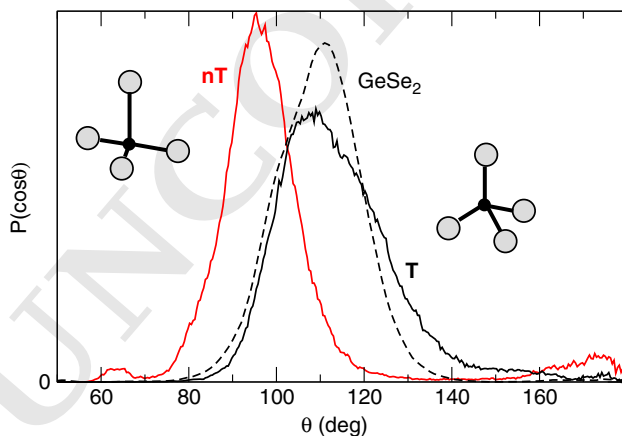


**Figure 7.** BAD of identified tetrahedral (T, black) and non-tetrahedral (nT, red) Ge in  $\text{GeTe}_2$ . Associated structures are represented. The broken curve corresponds to the Se—Ge—Se BAD in the isochemical  $\text{GeSe}_2$ .<sup>[24]</sup>

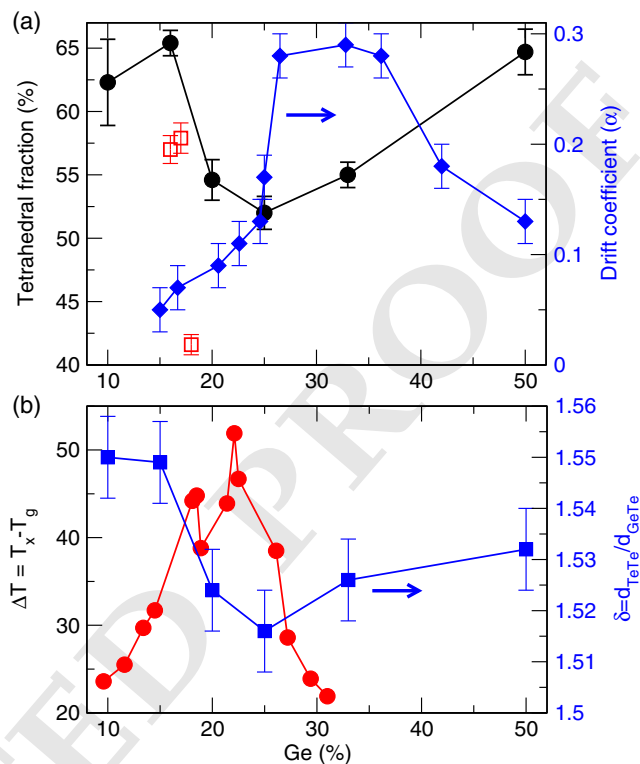


**Figure 8.** a) Evolution of the calculated tetrahedral fraction  $\eta(x)$  as a function of Ge content in amorphous  $\text{Ge}_x\text{Te}_{100-x}$  systems (see the previous studies,<sup>[10,14]</sup> and the present work). The red open symbols represent experimental numbers extracted from Mössbauer spectroscopy.<sup>[10]</sup> Right axis: Experimentally drift coefficient characterizing the time evolution (aging) of the resistivity (blue symbols).<sup>[42]</sup> b) Thermal stability  $\Delta T = T_x - T_g$  in  $\text{Ge}_x\text{Te}_{100-x}$ , measured by differential scanning calorimetry.<sup>[16]</sup> Right axis: Calculated ratio  $\delta = d_{\text{TeTe}}/d_{\text{GeTe}}$  as a function of Ge content (blue symbols).

with an measurement from Mössbauer spectroscopy. This exper- 1  
imental technique finds a (T) fraction  $\eta$  of about 57% around the 2  
eutectic composition  $\text{Ge}_{15}\text{Te}_{85}$ , prior to an important decrease 3  
close to  $\text{GeTe}_4$  ( $41.6 \pm 0.8$ <sup>[10]</sup>), which indicates that Ge atoms 4  
are then predominantly found in an octahedral geometry. 5  
While this fraction is not fully reproduced from our simulations, 6  
we do find that  $\eta(x)$  displays a minimum value for larger Ge con- 7  
tent, close to the  $\text{GeTe}_3$  composition ( $52\%$ ), and the structure of 8  
 $\text{GeTe}$  is dominated by tetrahedra ( $\eta = 64.7\%$ ). It is important to 9  
emphasize at this stage that the chosen electronic schemes alter 10  
dramatically the calculated value of  $\eta$  and DFT calculations, 11  
which do not consider a dispersion correction lead to values that 12  
are much lower ( $\eta = 41.2\%$ <sup>[14]</sup>), a result that is directly driven 13  
by increased (i.e., overestimated) Ge—Te bond lengths, which 14  
promote octahedral geometries. 15

An indirect evidence for the evolution of (T) population 16  
with Ge content is also provided by the ratio  $\delta = d_{\text{TeTe}}/d_{\text{GeTe}}$  that 17  
is calculated from the relevant partial pair correlation functions. 18  
This ratio usually serves to characterize the modification in 19  
tetrahedral bonding,<sup>[4]</sup> given that for perfect tetrahedral geometries, 20  
one can expect to have the ratio  $\delta_x$  of the vertex distance 21  
 $d_{\text{XX}}$  over the Ge—X distance  $d_{\text{GeX}}$  ( $X = \text{O}, \text{S}, \text{Se}$ ) to be: 22

1  $\delta = d_{XX}/d_{GeX} = \sqrt{8/3} = 1.63$ , which is fulfilled in tetrahedral  
2 selenides and sulfides,<sup>[26]</sup> whereas the same ratio in a perfect  
3 octahedral bonding is given by  $\delta = \sqrt{2} = 1.41$ . The departure  
4 from the value  $\sqrt{8/3}$ , thus, signals for certain systems a tetrahe-  
5 dral to octahedral conversion.<sup>[4]</sup> In the present tellurides, it is  
6 seen that  $\delta$  is found between the limiting values of 1.41 and  
7 1.63 (Figure 8b, right axis), which signals, indeed, that the  
8 Ge is found as a mixture of (T) and (O) populations.  
9 Interestingly, the minimum evolution of  $\eta$  with Ge content  
10 correlates directly with the one found for  $\delta$ , and the latter is  
11 essentially driven by a reduction in the domain  $\approx 20$ –35% Ge  
12 of the Te–Te bond distance defining the vertex of the polyhedra.  
13 An alternative means of analyzing the tetrahedral fraction is the  
14 consideration of the single Ge–Te bond length  $d_{GeTe}$ .<sup>[27]</sup> In the  
15 present tellurides, the change with composition is too small and  
16 appears to be weakly sensitive to Ge content as  $d_{GeTe}$  is always  
17 found between 2.63(9) and 2.65(4) Å.

18 **Figure 9** represents the different obtained Ge-centered BADs  
19 fulfilling six rigid angles. All are, indeed, centered around 109°,  
20 although one notices increased excursions at large  $\theta$  for the  
21 GeTe<sub>2</sub> and GeTe compositions. A convenient way to provide  
22 an increased characterization of the effect of composition is to  
23 interpret the BADs in terms of an effective potential  $U_{\text{eff}}(\theta)$ ,  
24 assuming that one has

$$P(\cos \theta) \propto \exp[U_{\text{eff}}(\theta)/k_B T] \quad (3)$$

25 as introduced in studies on liquid–liquid transitions of  
26 silica.<sup>[40]</sup> We, furthermore, assume that the effective potential

is harmonic with a compositional-dependent stiffness constant 1  
 $k_2$ , i.e.,  $U_{\text{eff}}(\theta) = \frac{1}{2}k_2(x)(\theta - \theta_0)^2$ , and  $\theta_0$  being the tetrahedral 2  
angle. Using Equation (3), we fit the represented BADs and 3  
extract a stiffness  $k_2$  that is now represented as a function of 4  
Ge content (Figure 9). Note that  $\theta_0$  is left as an adjustable param- 5  
eter, and the fits lead systematically to the values in the range 6  
110.0° – 112.3°, except for two compositions (GeTe<sub>2</sub> and 7  
GeTe), which needed an additional distribution of the form of 8  
Equation (3) because of the presence of a tail in the BAD at 9  
 $\theta \approx 130^\circ - 140^\circ$ . This second contribution involves an additional 10  
fitted mean angle obtained at  $\theta_0 = 124.9^\circ$  for GeTe (115.2° for 11  
GeTe<sub>2</sub>) and smaller stiffness  $k_2$ . The detailed analysis of the 12  
Ge-centered BADs shows that this contribution is associated with 13  
a Ge–Ge–Te BAD, and the emergence of such motifs is linked 14  
with the growing presence of homopolar bonds that have been 15  
detected from RMC simulations once  $x > 20\%$ .<sup>[25]</sup> The evolution 16  
of  $k_2$  for the main contribution (i.e., at 109°) with Ge content is 17  
compatible with the trend observed for the tetrahedral fraction 18  
(Figure 8) as large  $k_2$  values imply that more tetrahedra are 19  
present in the structure with small harmonic excursions 20  
away from 109°. The stiffness appears, however, to be much 21  
smaller than the one calculated from a trajectory of GeSe<sub>4</sub><sup>[24]</sup> 22  
where a similar fit on the Se–Ge–Se BAD leads to 23  
 $k_2 = 315.7 \text{ J mol}^{-1} \text{ deg}^{-2}$ , i.e., much larger than for the corre- 24  
sponding tellurides, and this selenide material is, indeed, made 25  
of 100% tetrahedra. 26

The presence of a minimum in tetrahedral fraction (Figure 8) 27  
and stiffness  $k_2$  in this compositional range (20–33%) has a link 28  
with a possible flexible to rigid transition but with features that 29

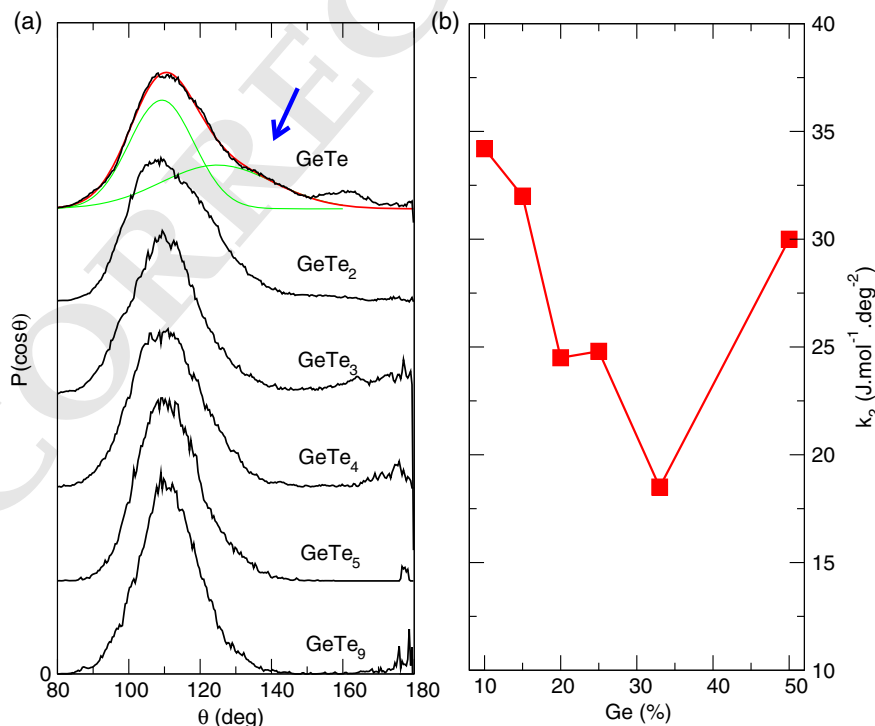


**Figure 9.** a) Calculated Ge-centered BADs  $P(\cos \theta)$  fulfilling six rigid angles for different compositions in Ge–Te binary. The thin red line represents a fit using Equation (3) over the 80° – 150° angular domain for GeTe, and green curves correspond to the two respective contributions centered at 109.2° and 124.9° (see text for details). b) Fitted stiffness  $k_2$  at  $\approx 109^\circ$  for the Ge-centered bond angle as a function of Ge content  $x$  in amorphous  $\text{Ge}_x\text{Te}_{100-x}$ .

1 turn out to be specific to tellurides, given that the fraction of tetra-  
2 hrahedra evolves with Ge content. Such transitions are being cur-  
3 rently observed for the other chalcogenides, e.g.,  $\text{Ge}_x\text{Se}_{100-x}$ <sup>[24]</sup>  
4 or  $\text{Ge}_x\text{S}_{100-x}$ <sup>[23]</sup>. At this transition, a certain number of physico-  
5 chemical properties display minima or maxima, and for  
6 selenides or sulfides, this transition point is located at  
7  $x_c = 20\%$ <sup>[33]</sup>. While this transition point at  $x_c$  can be predicted  
8 exactly from a mean-field treatment of radial and angular rigidity  
9 in such lighter chalcogenides where the octet rule applies,  
10 the uncertainties associated with the increased electronic  
11 delocalization of the bonding make the application of such  
12 theoretical methods more problematic in tellurides.

13 An inspection of Figure 8 indicates that the anomaly observed  
14 for  $\eta$  correlates with properties measured in the context of phase-  
15 change applications.

16 The evolution of the drift of the resistivity with Ge content  
17 appears to be related to the change in local geometry. This drift  
18 is usually described by a power law of the form  $\rho(t)/\rho_0 = (t/t_0)^\alpha$ ,  
19 where  $\rho_0$  is the resistivity at the initial time  $t_0$ , the exponent  $\alpha$   
20 characterizing the behavior with time.<sup>[41]</sup> Once represented as  
21 a function of Ge content (Figure 8a, right axis), one realizes  
22 qualitatively that PCM with a large amount of (T) geometries will  
23 display a smaller variation in resistivity (small  $\alpha$  values),  
24 and the abrupt change in  $\alpha(x)$  at  $x_c = 23\%$  is possibly related  
25 to a flexible to rigid transition.<sup>[42]</sup> The important increase in  
26 the drift coefficient resistivity at this rigidity threshold obviously  
27 reflects a higher tendency to aging for Ge-rich layers, and is  
28 also associated with the appearance of the homopolar Ge–Ge  
29 bonds.<sup>[25,43]</sup>

30 Figure 8b also shows some correlation with the fraction of tetra-  
31 hrahedra, and one acknowledges an enhanced thermal stability  
32  $\Delta T = T_x - T_g$  close to 22% Ge. Here,  $T_x$  is the temperature of crys-  
33 tallization onset, and  $T_g$  is the glass-transition temperature,<sup>[16]</sup>  
34 which reflects the ability of the material to vitrify, and  $\Delta T$  is  
35 maximum in the region where the population of both tetrahedra  
36 and defect octahedra is about the same.

37 Regarding the link between PC phenomena and local struc-  
38 ture/geometry, the picture that emerges from our analysis is  
39 the following. At large Ge content, apart (O) local geometries,  
40 (T) display two types of short range order: a first one that is,  
41 indeed, close to the value  $\arccos(-\frac{1}{3}) = 109.47^\circ$  and dominant  
42 at small composition  $x$  (Figure 9) where the effects of stress  
43 and presence of homopolar Ge–Ge bonds is negligible. With  
44 increasing Ge content, the rigidity induced from increased  
45 stress/bond density<sup>[33]</sup> is partially released by a global reduction  
46 of the (T) fraction to about  $\approx 50\%$  at  $\text{GeTe}_3$  (Figure 8a) as less  
47 angular rigid constraints are involved, because these evolve as  
48  $5\eta + 3(1-\eta) = 3 + 2\eta$ .<sup>[17]</sup> For larger concentration, the emergence  
49 of Ge–Ge bonds promotes back again (T) geometries,<sup>[6]</sup> and a  
50 second (T) contribution emerges at  $115 - 124^\circ$  that involves a  
51 homopolar bond and continues to have six rigid angles. It is  
52 already detected for  $\text{GeTe}_2$  (Figure 9). The deviation from a stan-  
53 dard tetrahedral angle to larger values is rather well known in the  
54 literature and found in strained molecules, such as, e.g., fenes-  
55 tranes,<sup>[44]</sup> a class of materials where the bond lengths deviate  
56 from those found in reference alkanes and induce a bond angle  
57 at the central carbon atom of around  $130^\circ$ . The mechanism of  
58 “planarization” of the tetrahedral carbon results of a gradual

increase in bond angle deformation and strain energy that effect  
a change in hybridization.<sup>[45]</sup> In the present tellurides, this sec-  
secondary (T) population appears to be an intermediate geometry  
between the regular (T) and the (O) geometry, promoted by  
the presence of stress.

The fact that the intratetrahedral bending motion is more soft  
in tellurides must have some implications for corresponding  
vibrational spectra as acknowledged, e.g., for the case of densified  
silicas.<sup>[46]</sup> In Ge–Te glasses,<sup>[42]</sup> the Raman spectra contain  
features of Te-sites but also signatures of Ge-based local geome-  
tries with typical frequencies of  $122 - 126$  and  $160 \text{ cm}^{-1}$  for  
defect octahedra and a broadband centered around  $190 \text{ cm}^{-1}$   
for tetrahedral.<sup>[47]</sup> Using an effective mass  $m$  for the vibrating  
structures (i.e., corresponding to the chalcogen mass, which is  
larger in the case of Te-based glasses), one can estimate the  
typical frequency of bending modes  $\omega_{\text{BB}} = \sqrt{\beta/m} \cos \theta/2$  from  
a nearest-neighbor central-force model.<sup>[48]</sup> It indicates that  
 $\omega_{\text{BB}}$  must be smaller in tellurides as the restoring force constant  
 $\beta$  must be lower in  $\text{GeTe}_y$ , due to the increased angular  
excursion, when compared with, e.g., selenides, which involve  
an increased frequency for bending motion<sup>[49]</sup> as also  
acknowledged for vibrational study of S/Se substitution in stoi-  
chiometric compounds.<sup>[50]</sup>

In the present contribution, DFT-based simulations, we have  
focused on the structure of  $\text{GeTe}_2$ , an isochemical compound of  
tetrahedral network formers of the form  $\text{GeX}_2$  ( $X = \text{O}, \text{S}, \text{Se}$ ).  
These simulations appear to reproduce rather accurately the  
overall structural properties of the amorphous phase, as  
acknowledged by a rather good agreement with experimental  
structure functions (structure factor  $S(k)$  and pair correlation  
functions  $g(r)$ ). We have then focused on the geometrical motif  
associated with Ge atoms and results that indicate a rather  
important fraction of tetrahedra (55%), but these appear to be  
soft units that experience angular excursions up to  $160^\circ - 170^\circ$   
during bond-bending motions. These excursions are larger than  
in corresponding sulfides and selenides whose short range order  
can be fairly described within a rigid unit model typical of oxide  
network formers ( $\text{GeO}_2, \text{SiO}_2$ ).

Once the fraction of tetrahedra is followed as a function of Ge  
content, a minimum is obtained close to a reported rigidity tran-  
sition, whereas Ge-rich compositions and  $\text{GeTe}$  appear to contain  
the largest population of tetrahedra but, in the last case, with a  
secondary geometry, related to the presence of Ge–Ge bonds,  
having a mean angle of about  $125^\circ$  that leads to a specific tail  
in the BAD at large angles. These trends permit to decode  
observed anomalies in properties regarding phase-change mech-  
anisms, and might be of some interest for further work in terms  
of applications. More generally, the ease of phase switching is  
directly linked to small ionicity and a limited degree of hybrid-  
ization, enabling some resonance p-electron bonding to prevail.  
This means that  $\text{sp}^3$  tetrahedral geometries involving occupied  
but energetically unfavorable  $\text{sp}^3$  antibonding states might lead  
to the absence of resonance bonding. The fact that such (T) units  
appear to be much softer than their selenide or sulfide counter-  
parts, able to explore larger angles and possible additional  
interactions, indicates that even tetrahedral tellurides can be  
promising candidates for PC applications.

Q5

## 1 Acknowledgements

2 The authors acknowledge support from Agence Nationale de la Recherche  
3 (ANR) (Grant No. ANR-11-BS08-0012).

## 4 Conflict of Interest

5 The authors declare no conflict of interest.

## 6 Keywords

7 ab initio simulation, bond angle distribution, geometrical motifs, phase-  
8 change materials

9 Received: October 14, 2020

10 Revised: November 6, 2020

11 Published online:

- [20] P. S. Salmon, A. C. Barnes, R. A. Martin, G. J. Cuello, *J. Phys.: Condens. Matter* **2007**, *19*, 415110. 1  
2
- [21] A. Bychkov, C. J. Cuello, S. Kohara, C. J. Benmore, D. L. Price, E. Bychkov, *Phys. Chem. Chem. Phys.* **2013**, *15*, 8487. 3  
4
- [22] P. S. Salmon, J. Non-Cryst. Solids **2007**, *353*, 2959. 5
- [23] S. Chakraborty, P. Boolchand, M. Micoulaut, *Phys. Rev. B* **2017**, *96*, 094205. 6  
7
- [24] M. Micoulaut, A. Kachmar, M. Bauchy, S. Le Roux, C. Massobrio, M. Boero, *Phys. Rev. B* **2013**, *88*, 054203. 8  
9
- [25] A. Piarristeguy, M. Micoulaut, R. Escalier, P. Jávári, I. Kaban, J. van Eijk, J. Luckas, S. Ravindren, P. Boolchand, A. Pradel, *J. Chem. Phys.* **2015**, *143*, 074502. 10  
11
- [26] P. S. Salmon, A. Zeidler, *J. Stat. Mech.* **2019**, 114006. 13
- [27] J. R. Stellhorn, S. Hosokawa, W.-C. Pilgrim, N. Blanc, N. Boudet, H. Tajiri, S. Kohara, *Phys. Status Solidi* **2016**, *253*, 1038. 14  
15
- [28] M. Micoulaut, *J. Phys. Condens. Matter.* **2019**, *31*, 285402. 16
- [29] S. Hosokawa, K. Tamura, M. Inui, H. Endo, *J. Non-Cryst. Solids* **1993**, *156–158*, 712. 17  
18
- [30] I. Kaban, P. Jávári, W. Hoyer, R. G. Delaplane, A. Wannberg, *J. Phys. Cond. Matt.* **1993**, *18*, 2749. 19  
20
- [31] J. Akola, R. O. Jones, *Phys. Rev. B* **2007**, *76*, 235201. 21
- [32] M. Bauchy, M. Micoulaut, *J. Non-Cryst. Solids* **2011**, *357*, 2530. 22
- [33] M. Micoulaut, *Adv. Physics X* **2016**, *1*, 147. 23
- [34] M. Bauchy, M. Micoulaut, M. Celino, M. Boero, S. Le Roux, C. Massobrio, *Phys. Rev. B* **2011**, *84*, 054201. 24  
25
- [35] M. Bauchy, M. Micoulaut, M. Boero, C. Massobrio, *Phys. Rev. Lett.* **2013**, *110*, 165501. 26  
27
- [36] M. Bauchy, M. J. Abdolhosseini Qomi, C. Bichara, F.-J. Ulm, R. J.-M. Pellenq, *J. Phys. Chem. C* **2014**, *118*, 12485. 28  
29
- [37] M. Dove, K. Hammonds, M. Harris, V. Heine, *Mineral. Mag.* **2000**, *64*, 377. 30  
31
- [38] O. Laurent, B. Mantsi, M. Micoulaut, *J. Phys. Chem. B* **2014**, *118*, 12750. 32  
33
- [39] M. Micoulaut, C. Otjacques, J.-Y. Raty, C. Bichara, *Phys. Rev. B* **2010**, *81*, 174206. 34  
35
- [40] E. Lascaris, M. Hemmati, S. V. Buldyrev, H. E. Stanley, C. A. Angell, *J. Chem. Phys.* **2014**, *140*, 224502. 36  
37
- [41] M. Boniardi, A. Redaelli, A. Pirovano, I. Tortorelli, F. Pellizzer, *J. Appl. Phys.* **2009**, *105*, 084506. 38  
39
- [42] J. Luckas, A. Olk, P. Jost, H. Volker, J. Alvarez, A. Jaffré, P. Zalden, A. Piarristeguy, A. Pradel, C. Longeaud, M. Wuttig, *Appl. Phys. Lett.* **2014**, *105*, 092108. 40  
41  
42
- [43] A. V. Kolobov, P. Fons, J. Tominaga, *Phys. Rev. B* **2013**, *87*, 155204. 43
- [44] V. B. Rao, C. F. George, S. Wolff, W. C. Agosta, *J. Am. Chem. Soc.* **1985**, *107*, 573. 44  
45
- [45] R. Keese, *Chem. Rev.* **2006**, *106*, 4787. 46
- [46] B. Hehlen, *J. Phys. Cond. Matt.* **2010**, *22*, 022401. 47
- [47] R. Mazzarello, S. Caravati, S. Angioletti-Uberti, M. Bernasconi, M. Parrinello, *Phys. Rev. Lett.* **2010**, *104*, 085503. 48  
49
- [48] P. N. Sen, M. F. Thorpe, *Phys. Rev. B* **1977**, *15*, 4030. 50
- [49] P. Boolchand, W. J. Bresser, *Phil. Mag.* **2000**, *80*, 1757. 51
- [50] X. Han, H. Tao, L. Gong, X. Wang, X. Zhao, Y. Yue, *J. Non-Cryst. Solids* **2014**, *391*, 117. 52  
53
- [51] A. Zeidler, W. E. Drewitt, P. S. Salmon, A. C. Barnes, W. A. Crichton, S. Klotz, H. E. Fischer, C. J. Benmore, S. Ramos, A. C. Hannon, *J. Phys.: Condens. Matter* **2006**, *21*, 474217. 54  
55  
56

- [1] W. Zhang, R. Mazzarello, M. Wuttig, E. Ma, *Nature Rev. Mat.* **2019**, *4*, 150. 12  
13
- [2] *Phase Change Materials And Applications*, (Eds: S. Raoux, M. Wuttig), Springer, Berlin **2008**. 14
- [3] A. V. Kolobov, P. Fons, A. I. Frenkel, A. L. Ankudinov, J. Tominaga, T. Uruga, *Nat. Mater.* **2004**, *3*, 703. 15  
16
- [4] M. Micoulaut, *J. Phys.: Condens. Matter* **2004**, *16*, L131. 17
- [5] D. A. Baker, M. A. Paesler, G. Lucovsky, S. C. Agarwal, P. C. Taylor, *Phys. Rev. Lett.* **2006**, *96*, 255501. 18  
19
- [6] J.-Y. Raty, W. Zhang, J. Luckas, C. Chen, R. Mazzarello, C. Bichara, M. Wuttig, *Nat Commun* **2015**, *6*, 7467. 20  
21
- [7] J. Akola, R. O. Jones, *Phys. Rev. Lett.* **2008**, *100*, 205502. 22
- [8] S. Gabardi, S. Caravati, G. C. Sosso, J. Behler, M. Bernasconi, *Phys. Rev. B* **2015**, *92*, 054201. 23  
24
- [9] S. Caravati, M. Bernasconi, M. Parrinello, *J. Phys.: Condens. Matter* **2010**, *22*, 315801. 25  
26
- [10] M. Micoulaut, K. Gunasekera, S. Ravindren, P. Boolchand, *Phys. Rev. B* **2014**, *90*, 094207. 27  
28
- [11] M. Micoulaut, *J. Chem. Phys.* **2013**, *138*, 061103. 29
- [12] M. Micoulaut, M.-V. Coulet, A. Piarristeguy, M. R. Johnson, G. J. Cuello, C. Bichara, J.-Y. Raty, H. Flores-Ruiz, A. Pradel, *Phys. Rev. B* **2014**, *89*, 174205. 30  
31  
32  
33
- [13] H. Flores-Ruiz, M. Micoulaut, M.-V. Coulet, A. A. Piarristeguy, M. R. Johnson, G. J. Cuello, A. Pradel, *Phys. Rev. B* **2015**, *92*, 134205. 34  
35
- [14] M. Micoulaut, A. Piarristeguy, H. Flores-Ruiz, A. Pradel, *Physical Review B* **2017**, *96*, 184204. 36  
37
- [15] A. Bouzid, C. Massobrio, M. Boero, G. Ori, K. Sykina, E. Furet, *Phys. Rev. B* **2015**, *92*, 134208. 38  
39
- [16] P. Jávári, A. Piarristeguy, R. Escalier, I. Kaban, J. Bednarcik, A. Pradel, *J. Phys. Condens. Matter* **2013**, *25*, 195401. 40  
41
- [17] K. Gunasekera, P. Boolchand, M. Micoulaut, *J. Appl. Phys.* **2014**, *115*, 164905. 42  
43
- [18] J. Akola, R. O. Jones, S. Kohara, T. Usuki, E. Bychkov, *Phys. Rev. B* **2010**, *81*, 094202. 44  
45
- [19] S. Grimme, *J. Comput. Chem.* **2006**, *27*, 1787. 46